ENGINEERING

Programmed shape-morphing into complex target shapes using architected dielectric elastomer actuators

Ehsan Hajiesmaili[1]*, Natalie M. Larson[1,2], Jennifer A. Lewis[1,2], David R. Clarke[1]

Dielectric elastomer actuators (DEAs) are among the fastest and most energy-efficient, shape-morphing materials. To date, their shapes have been controlled using patterned electrodes or stiffening elements. While their actuated shapes can be analyzed for prescribed configurations of electrodes or stiffening elements (the forward problem), the design of DEAs that morph into target shapes (the inverse problem) has not been fully addressed. Here, we report a simple analytical solution for the inverse design and fabrication of programmable shape-morphing DEAs. To realize the target shape, two mechanisms are combined to locally control the actuation magnitude and direction by patterning the number of local active layers and stiff rings of varying shapes, respectively. Our combined design and fabrication strategy enables the creation of complex DEA architectures that shape-morph into simple target shapes, for instance, those with zero, positive, and negative Gaussian curvatures as well as complex shapes, such as a face.

INTRODUCTION

Animal locomotion, optimized over millions of years of evolution, involves complex motions and shape changes. Bat wings, for example, reduce drag forces during upstroke by twisting and folding their wings and increase lift during downstroke by keeping the leading-edge vortices attached to the wing using complex shape changes generated by more than two dozen joints and highly deformable bones that are overlaid by thin elastic membranes and muscles (*1*), or when a bluegill sunfish swims, its pectoral fin twists, bends chordwise and spanwise, and morphs into a cupped shape during abduction (*2*). Biomimicry of this complex locomotion is an elegant engineering solution for high-performance robots, but this requires actuators that produce these complex shape changes with power densities akin to skeletal muscles and inverse design tools that predict the architecture of shape-morphing actuators needed to generate targeted complex shape changes.

Dielectric elastomer actuators (DEAs) (*3*) have enabled several examples of bio-inspired locomotion, including artificial muscles with performance akin to human muscles (*4*), flying wing-flapping robots that withstand mechanical impacts and collisions (*5*), swimming robots that tolerate high hydrostatic pressures with prospective for deep-sea explorations (*6*), and soft crawling and climbing inchworm robots (*7*, *8*). DEAs are soft capacitors that, in their simplest configuration, consist of dielectric elastomer layers coated by compliant electrodes. When subjected to a voltage, each dielectric layer is squeezed in thickness in response to the attractive Coulombic forces between oppositely charged electrodes and expanded laterally due to its incompressibility. A multilayer stack of elastomer dielectric layers and interdigitated electrodes gives rise to linear actuations of interest for applications, such as artificial biceps (*4*). Alternately, bending actuations necessary for crawling and swimming robots (*6*–*8*) can be generated by attaching a so-called passive layer to the active DEA thin sheet. Linear and bending actuations are the predominant modes observed for DEAs to date. However, the potential design space for creating novel devices that exhibit more sophisticated forms of actuation is very large. For example, DEAs can be used to create tunable optical lenses that change their focal length via curvature morphing (*9*).

Localized controlled actuations are the basis of generalizable shape-morphing actuators. For example, hydrogel-based shape-morphing architectures have been fabricated that harness differential shrinkage (*10*) or swelling of *N*-isopropylacrylamide polymer encoded with localized stiffness anisotropy using biomimetic four-dimensional (4D) printing (*11*) or halftone gel lithography (*12*). Elastomer-based shape-morphing architectures have also been developed including those based on pneumatic inflation that contain a specific network of embedded airways (*13*) and multimaterial lattices with locally controlled stiffness and coefficients of thermal expansion (*14*). Each of these actuators exhibits spatially distributed deformations that are essential for changing the Gaussian curvature field. The inverse design problems for these shape changes were addressed to determine the actuator designs that morph into desired target shapes. These solutions are specific to their actuation mechanisms and produce actuation shapes that approximate the target shapes within reasonable ranges of error, e.g., maximum error of 8 mm for the out-of-plane displacement for an actuator morphing from flat into a human face with a maximum height difference of 30 mm and lateral dimensions of 112 mm by 165 mm (*14*). The shape-morphing actuators based on temperature changes or swelling require altering the environment surrounding the actuator and show relatively slow actuation speeds on the order of 0.01 Hz [see, for example, movie S1 in (*14*)], making them unsuitable for robotic applications such as swimming and flying locomotion that require high-speed shape changes and imperviousness to the surrounding environment. The pneumatic shape-morphing actuators can provide high actuation strains and forces and have higher frequency responses; however, their actuations require pneumatic pumps and tubing and additionally their large thicknesses, e.g., 3.8 to 6.7 mm (*13*), preventing them from being used as artificial membrane muscles.

DEAs are outstanding candidates for creating shape-morphing actuators for robotics applications since they can be addressed using

[1]John A. Paulson School of Engineering and Applied Sciences, Harvard University, Cambridge, MA 02138, USA. [2]Wyss Institute for Biologically Inspired Engineering, Harvard University, Cambridge, MA 02138, USA.
*Corresponding author. Email: hajiesmaili@seas.harvard.edu

applied voltages and, imperviously to their environment parameters such as temperature, they provide fast and reversible actuations with frequency responses up to 1 kHz (*5*), high energy densities, e.g., 19.8 J/kg, which are on a par with natural muscles (0.4 to 40 J/kg), and relatively high energy conversion efficiencies (*15*). DEAs have relied on two methods for shape-morphing (*16*, *17*): one based on spatially controlling the magnitude of equi-biaxial actuations through the design of interdigitated electrodes in multilayer structures with varying number of layers (*16*) and another based on controlling local actuation directions using, for example, stiff rings patterned by extrusion-based 3D printing (*17*). Simple shape-morphing actuators have been demonstrated using these two methods, such as dome-like, saddle-like, and torus-like shapes, cones, and anti-cones. The forward problem of modeling the actuation shape given a design of the electrodes and stiff rings has been successfully demonstrated using nonlinear finite elements method (*3*, *18*).

Creating more complex actuation shapes requires inverse design to identify the optimum layout of the electrodes and stiffener elements, such as rings, so that the fabricated DEAs shape-morph into a desired target shape when subjected to an applied voltage. Topology optimization methods (*19*) are often adopted for such problems. For instance, to maximize in-plane displacement of several discrete points on a prestretched DEA thin sheet, the level-set method has been used to optimize the internal electric fields (*20*). Recently, Martínez-Frutos *et al.* (*21*) have developed a novel topology optimization method to optimize electrode mesoarchitectures that maximize and minimize the out-of-plane displacements of several points on a shape-morphing DEA. Separately, Ortigosa and Martínez-Frutos (*22*) have developed a method to optimize the layout of stiffening elements for shape-morphing DEAs based on solid isotropic material with penalization. Analytical solutions of the inverse problem are possible when more local degrees of freedom for the local actuation are controllable. For instance, a bilayer soft actuator can be exactly morphed into any target shape using an analytical solution to the inverse problem, provided that the actuation of both layers can be controlled in both directions (*23*). Such analytical solutions are preferable to the topological optimization methods, which are, by nature, iterative. The latter can also be prohibitively computationally expensive for larger-scale problems, and the results depend on the starting designs of the optimizations.

Here, we present an integrated inverse design and fabrication method for creating architected DEAs that rapidly and reversibly shape-morph into predefined target shapes by locally controlling their actuation magnitudes and directions. In the following sections, first, the structure of the shape-morphing DEAs that allow for the local control of actuation magnitudes and directions is introduced. Then, an analytical solution for the inverse problem is presented, leveraging the local control of actuation magnitudes and directions. Next, morphing of a flat sheet into mathematically well-defined shapes, including cones and axisymmetric sinusoidal and cosine caps, is demonstrated, having a maximum slope of 29°, corresponding to 10% actuation strain of the particular elastomer used. Subsequently, morphing into more complex shapes is discussed using an example of morphing into the shape of a human face. The assumptions and limitations of this shape-morphing method are discussed. The paper concludes with a discussion of merits and potential applications of analytically designed shape-morphing DEAs, as well as the limitations to be addressed in future works.

RESULTS

Shape-morphing DEAs with locally controlled actuation directions and magnitudes

Flat sheets of elastomer can be morphed into predefined target shapes, as will be shown in the following, when both the local actuation directions and magnitudes are controlled. Figure 1A presents an exploded view schematic of the architecture of a shape-morphing DEA designed to morph into a hemispherical cap shown in Fig. 1B. To control the local in-plane actuation direction, stiff rings of varying geometry are 3D-printed onto the surface of the multilayer elastomer sheet. The high stiffness of the rings (fig. S1B), relative to the elastomer (fig. S1A), constrains the deformations so that the actuations are locally uniaxial and normal to the rings. For the shape-morphing DEA example shown in Fig. 1A, the rings are concentric circles constraining the hoop deformations and only allowing radial actuations. To control the local actuation magnitudes, the shape-morphing DEAs are designed to have multilayer structures with interdigitated electrodes and the local actuation magnitudes are controlled by the local number of active layers. A layer is responsive to the local electric field in the region where the adjacent electrodes overlap. The distribution of the number of active layers, therefore, determines the design of the electrodes. For the shape-morphing DEA example shown in Fig. 1A, for instance, there are three active layers near the edge of the circular elastomer disk, causing larger deformations around the edge. Moving toward the center of the disk, the number of active layers reduces to zero, so that there is no actuation near the center.

Analytical solution of the inverse problem

For a desired target shape, the analytical solution to the inverse problem determines the pattern of the stiffening elements and the design of the electrodes on each layer. Deformation mappings that morph a flat sheet into a target shape are nonunique. To morph an initially flat sheet, defined by (X, Y, and $Z = 0$), into a target shape, defined by (x, y, $z(x, y)$), the deformation mapping is chosen such that the lateral displacements are zero, $x = X$, and $y = Y$, and the out-of-plane displacement is $z = z(X, Y)$ (Fig. 1B). This choice of the mapping imposes zero change in length along the contour lines of constant $z(X, Y)$, while maximizing the change in length normal to that, i.e., along the gradient vector $\vec{\nabla} z(X, Y)$. In other words, the actuations are locally uniaxial with the first principal stretch λ_1 being along the gradient vector $\vec{\nabla} z(X, Y)$ and the second principal stretch $\lambda_2 = 1$ along the contour lines. For the example of morphing into a spherical cap of Fig. 1B, the arrows in Fig. 1C (left) show the required distribution of in-plane actuation directions.

The distribution of in-plane actuation directions is provided by the pattern of 3D-printed stiff rings. Since, on one hand, the mapping is chosen such that the actuations are uniaxial normal to the contour lines of $z(X, Y)$ and, on the other hand, the stiff rings create locally uniaxial actuations normal to the rings, the pattern of the 3D-printed rings must be the same as the contour lines of $z(X, Y)$. An infinite number of infinitely thin and stiff rings can exactly reproduce this uniaxial actuation field. In practice, however, the continuous distribution of actuation directions can only be approximated with a finite number of stiff rings. For example, Fig. 1C (right) shows how a set of concentric circular rings is used to regenerate the uniaxial radial actuations in Fig. 1C (left).

For the deformation mapping chosen in this work, the distribution of the actuation magnitude λ_1 can be determined from the relative change in local surface area using the first fundamental

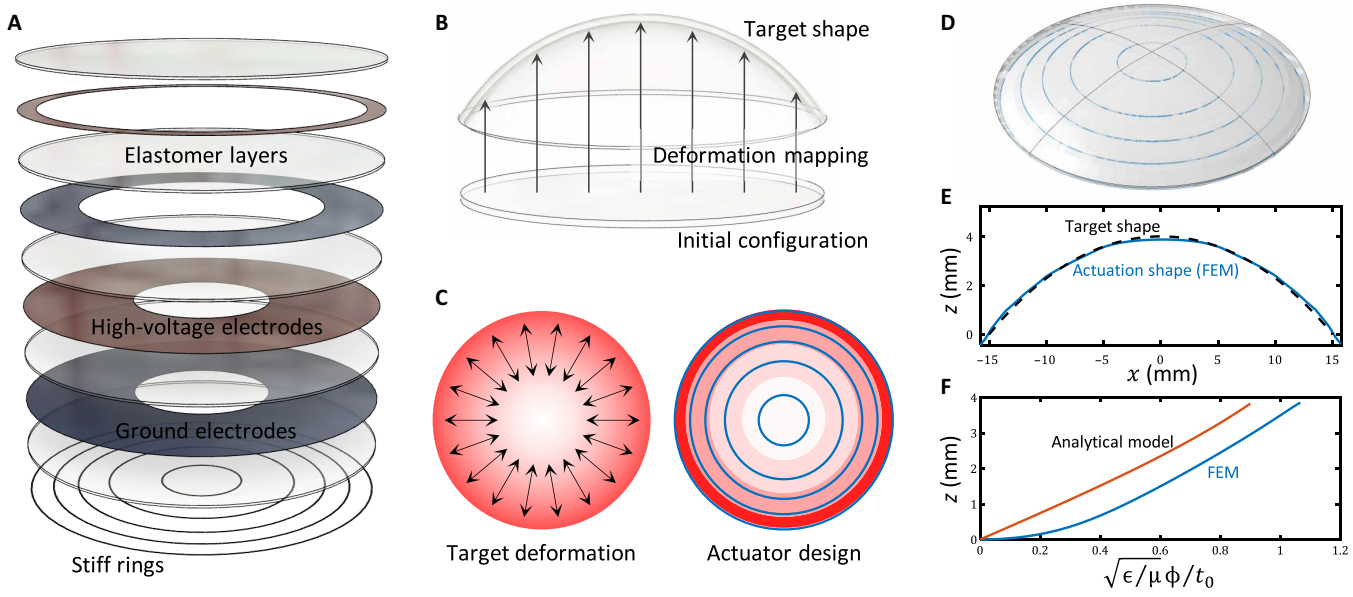

Fig. 1. Schematic and simulation of a shape-morphing DEA designed to morph into a hemispherical cap. (**A**) Schematic exploded view of the structure of the shape-morphing DEA, designed to morph into a hemispherical cap, consisting of a multilayer of elastomers, separated by interdigitated ground and high-voltage electrodes, and a set of stiff rings that are 3D-printed onto the multilayer. (**B**) The initially flat elastomer sheet morphs into a hemispherical shape through a deformation mapping with zero lateral displacements and predefined out-of-plane displacement. (**C**) The deformation mapping (left) for morphing into the spherical cap consists of uniaxial actuations that are locally uniaxial along the radial direction, and their magnitude increases from zero at the center of the elastomer disk to the maximum at the edge. This target deformation is approximated by a set of stiff rings and active layers (right). Actuations along the rings are prevented, producing locally uniaxial deformations normal to the rings, and the number of active layers determines the local magnitude of actuation. (**D**) The actuation shape for the actuator design in (A), simulated using finite element method (FEM), resembles the hemispherical target shape. (**E**) Quantitative comparison between the finite element simulation of the actuation profile and the target shape. (**F**) Finite element simulation of the displacement of the center of the disk as a function of the nondimensionalized electric potential shows that a critical strain is required for the DEA to buckle out of plane and morph in a 3D shape, resulting in a shift in nondimensionalized electric potential.

form of the surface (*24*). The relative change in surface area is $da/dXdY = \sqrt{EG - F^2} = \sqrt{(\partial z/\partial X)^2 + (\partial z/\partial Y)^2 + 1} = \sqrt{|\vec{\nabla} z(X,Y)|^2 + 1}$, where $E = \partial(x, y, z)/\partial X.\ \partial(x, y, z)/\partial X$, $F = \partial(x, y, z)/\partial X.\ \partial(x, y, z)/\partial Y$, and $G = \partial(x, y, z)/\partial Y.\ \partial(x, y, z)/\partial Y$. Since $\lambda_2 = 1$, the relative change in surface area is $da/dXdY = \lambda_1\lambda_2 = \lambda_1$, and therefore, $\lambda_1 = \sqrt{|\vec{\nabla} z(X,Y)|^2 + 1}$. That is, the local magnitude of the uniaxial actuation λ_1 is nonlinearly proportional to the gradient vector $\vec{\nabla} z(X, Y)$. The shades of red in Fig. 1C (left) shows the required actuation distribution for morphing into the spherical cap of Fig. 1B.

For the multilayer shape-morphing DEA schematically shown in Fig. 1A, locally, the first principal actuation stretches λ_1, normal to the stiff rings, are the same as that of a uniaxial actuator, if the bending stiffnesses and moments are ignored. Therefore, with a neo-Hookean model, the local actuation magnitude can be expressed as a function of the normalized electric potential $\hat{\phi}$ as $\lambda_1 = (1 - \hat{\phi}^2)^{-1/4}$ (*3*). The nondimensionalized electric potential can be locally controlled with the number of active layers n_a as $\hat{\phi} = \sqrt{n_a/N}\,\hat{\phi}_{\max}$, where N is the total number of layers and $\hat{\phi}_{\max} = \sqrt{\epsilon/\mu}\,\phi/t_0$ in which ϕ is the required voltage and ϵ, μ, and t_0 are the electrical permittivity, shear modulus, and initial thickness of each elastomer layer, respectively. The local number of active layers, therefore, is a function of the local magnitude of the gradient vector of the target shape $\vec{\nabla} z(X, Y)$ as

$$n_a(x,y) = \frac{N}{\hat{\phi}_{\max}^2}\left(1 - \left(|\vec{\nabla} z(x,y)|^2 + 1\right)^{-2}\right) \quad (1)$$

$\hat{\phi}_{\max}$ is determined from the maximum of the stretch distribution as $\lambda_{1,\max} = \left(1 - \left(1 - 2/N\right)\hat{\phi}_{\max}^2\right)^{-1/4}$, considering that the outer encapsulating layers are inactive. This leads to n_a ranging between 0 and $N - 2$ (Fig. 1A). Without the two encapsulating layers, the relation is $\lambda_{1,\max} = \left(1 - \hat{\phi}_{\max}^2\right)^{-1/4}$. Since the number of active layers must be an integer, $n_a(x, y)$ is rounded to the nearest integer. An infinite number of infinitely thin elastomer layers can exactly regenerate the distribution of the actuation magnitudes. In practice, however, the continuous distribution of actuation magnitudes can only be approximated by a discrete number of active layers. The discrete shades of red in Fig. 1C (right), for example, show the distribution of the active layers, approximating the continuous actuation magnitude of Fig. 1C (left).

To design, fabricate, and then evaluate the shape-morphing DEAs, a MATLAB code was developed with target shapes, material properties, and total number of layers and rings as inputs, and the design of the electrodes and the pattern of the stiff rings to be 3D-printed as outputs. The code is provided in the Supplementary Materials. The fabrication process of the shape-morphing DEAs is also described in detail in the Supplementary Materials. Briefly, elastomer layers are made by spin coating and ultraviolet (UV) curing of a urethane acrylate precursor followed by stamping of carbon nanotube (CNT) electrodes, created using a vacuum filtration method. The procedure is repeated for the number of layers of the multilayer shape-morphing DEA. To characterize the actuation performance of the DEA elastomer and electrodes, fig. S1C shows the uniform equi-biaxial actuation of a multilayer DEA with identical electrodes on all layers and no

3D-printed stiff rings. The stiff rings were deposited onto the DEA surface by direct ink writing of a viscoelastic acrylate–based ink. Immediately following ink deposition along the prescribed print path, the printed features were UV-cured under flowing argon. The shear modulus of the 3D-printed filaments (1.17 GPa; fig. S1B) is more than three orders of magnitude larger than that of the elastomer (327 kPa; fig. S1A). The width and height of the filaments, 0.20 and 0.05 mm, respectively, are nearly one order of magnitude smaller than the average spacing between the filaments (1 and 2 mm) and the total thickness of the elastomers (0.72 mm) for the shape-morphing DEAs demonstrated in the following.

Nonlinear finite element analysis (FEA) (*3*), which had previously been shown to give excellent agreement with actuation profile measurements (*16*, *17*), was used here to verify the design of the shape-morphing DEAs before their fabrication and to examine the validity of the assumptions and approximations of the presented shape-morphing method. Figure 1D shows the finite element simulation for the actuation profile of the shape-morphing DEA of Fig. 1A, a 1-mm-thick flat disk of elastomer, 15 mm in diameter, designed to morph into a hemispherical cap (Fig. 1B), with a radius of curvature of 30 mm. As the voltage applied to the interdigitated electrodes increases, the flat sheet of elastomer gradually deforms out of plane, and, at $\sqrt{\epsilon/\mu}\,\phi/t_0 = 1.08$, the actuation shape closely matches the target shape as shown in the comparison in Fig. 1E. However, the voltage at which the actuation shape is achieved differs from the voltage from the analytical model, $\sqrt{\epsilon/\mu}\,\phi/t_0 = 0.92$. Figure 1F, showing the out-of-plane displacement of the center of the DEA as a function of the nondimensionalized electric potential, explains the reason for this difference: the initially flat elastomer sheet requires a critical strain, at about $\sqrt{\epsilon/\mu}\,\phi/t_0 = 0.2$, to buckle out of plane and morph into a 3D shape. Following the out-of-plane buckling, the analytical model closely follows the finite element simulation, with a linear shift with the nondimensionalized voltage. Since mechanical inhomogeneities and anisotropies are incorporated into the shape-morphing DEAs, morphing into two fundamentally different shapes with one shape-morphing DEA, i.e., reconfigurability, is not possible. Adjusting the applied voltage results in the actuation shapes that are the same as the target shape but scaled in the height direction.

Axisymmetric target shapes: Cone, cosine, and sinusoidal shapes

Any shape can be characterized by its Gaussian curvature distribution as the intrinsic characteristic of the surface, and therefore, being able to morph into target shapes with zero, positive, and negative Gaussian curvatures is key for shape-morphing actuators. This section demonstrates shape-morphing DEAs that are designed to actuate into well-defined target shapes with zero, positive, and negative Gaussian curvatures. These include conical shape defined by $z(x,y) = A(1 - \sqrt{x^2 + y^2}/R)$ for the zero curvature, a cosine cap defined by $z(x,y) = A\cos\pi\sqrt{x^2 + y^2}/2R$ for the positive curvature, and a sinusoidal shape defined by $z(x,y) = A\sin\pi\sqrt{x^2 + y^2}/R$ for the negative curvature, in which A and R are the maximum out-of-plane displacements and the radii of the initially flat elastomer disks, respectively. For the ease of fabrication, R was chosen to be 15 mm. The actuation amplitude A was chosen such that the maximum actuation strain remained below 10%, above which electrical breakdown can occur for the material composition used (fig. S2).

For the zero-curvature conical shape (Fig. 2A, column I), the contour lines of constant $z(x, y)$ and therefore the stiff rings are concentric circles, the local actuations being in radial direction. The magnitude of the gradient vector $|\nabla z(x, y)|$ for the conical shapes is constant $|\nabla z| = A/R$, leading to a uniform number of active layers everywhere on the actuator as expected for a zero-curvature target shape. The design of the DEA to morph into conical shape is shown schematically in Fig. 2B (column I, left). It consists of a constant number of active layers, represented by the constant color intensity, that produce locally uniaxial actuations in the radial direction, represented by the black arrows. This actuation is created by the DEA shown in the image in Fig. 2B (column I, right), consisting of 12 layers ($n_a = 10$) and 10 rings. When the voltage is applied, the flat actuator morphs into the target cone shape as designed (Fig. 2C, column I). The actuation profile closely matches the target shape except at the apex of the cone where the singular point of the target shape is approximated by a rounded tip. The voltage at which the target conical shape with $A = 6$ mm is achieved (2.1 kV) is shifted from the calculated voltage using the analytical model (1.9 kV), once again due to the required critical actuation to buckle out of plane and morph into a 3D shape. The forward problem of DEAs with uniform actuation magnitude and 3D-printed concentric stiff rings morphing into conical shapes has been studied previously, showing the shift in voltage (*17*), the nearly zero Gaussian curvature everywhere except near the apex [see figure 2 in (*17*)], and the insensitivity of the actuation shape to the number of rings [see figures 3 and 4 in (*17*)].

For the positive curvature cosine cap [Fig. 2A, column II], the contour lines, and hence the layout of the stiff rings, are also concentric circles. The magnitude of the gradient vector increases with radius, from zero at the center to the maximum of $\pi A/2R$ toward the edge as $|\nabla z(x,y)| = \frac{\pi A}{2R}\sin\pi\sqrt{x^2 + y^2}/R$. This continuous radial actuation (Fig. 2B, column II, left) is created using a DEA with 12 layers and 10 rings (Fig. 2B, column II, right). The color intensity in Fig. 2B (column II, left), showing the required number of active layers to exactly reproduce the target deformation field, matches that of Fig. 2B (column II, right), representing the number of overlapping CNT electrodes. The design of each electrode is presented in fig. S3. When voltage is applied to the electrodes' interconnects, the DEA morphs into a cosine cap (Fig. 2C, column II, top). Comparing the actuation profile and the target shape shows their remarkable agreement (Fig. 2C, column II, bottom). The actuation shape is achieved at a slightly higher voltage of 2.1 kV than the 2.0 kV calculated from the analytical model, a difference attributed again to the initial buckling of the actuator. Movie S1 shows reversible morphing into the cosine shape at 1 Hz.

For the negative curvature sinusoidal shape (Fig. 2A, column III), the layout of the stiff rings is also found to be a set of concentric circles, creating locally radial actuation. The magnitude of the gradient vector has a maximum of $\pi A/R$ at the center and near the edge and a minimum of zero at $R/2$ from the center: $|\nabla z(x,y)| = \frac{\pi A}{R}\cos\pi\sqrt{x^2 + y^2}/R$. Figure 2B (column III, left) shows the actuation direction and number of active layers when $N \to \infty$, compared to the fabricated DEA in Fig. 2B (column III, right) that approximately generates this target actuation field using 12 layers and 10 rings. The actuation shape is shown in Fig. 2C (column III, top) and is compared to the target shape in Fig. 2C (column III, bottom). The design of each electrode is shown in fig. S4. The larger number of active layers at the center leads to separated islands of electrodes that are bridged to the electrode interconnects using 1-mm-wide CNT channels. (We note that these added bridges do not cause any notable change in the actuation shape, as shown in fig. S4C, due to their negligible

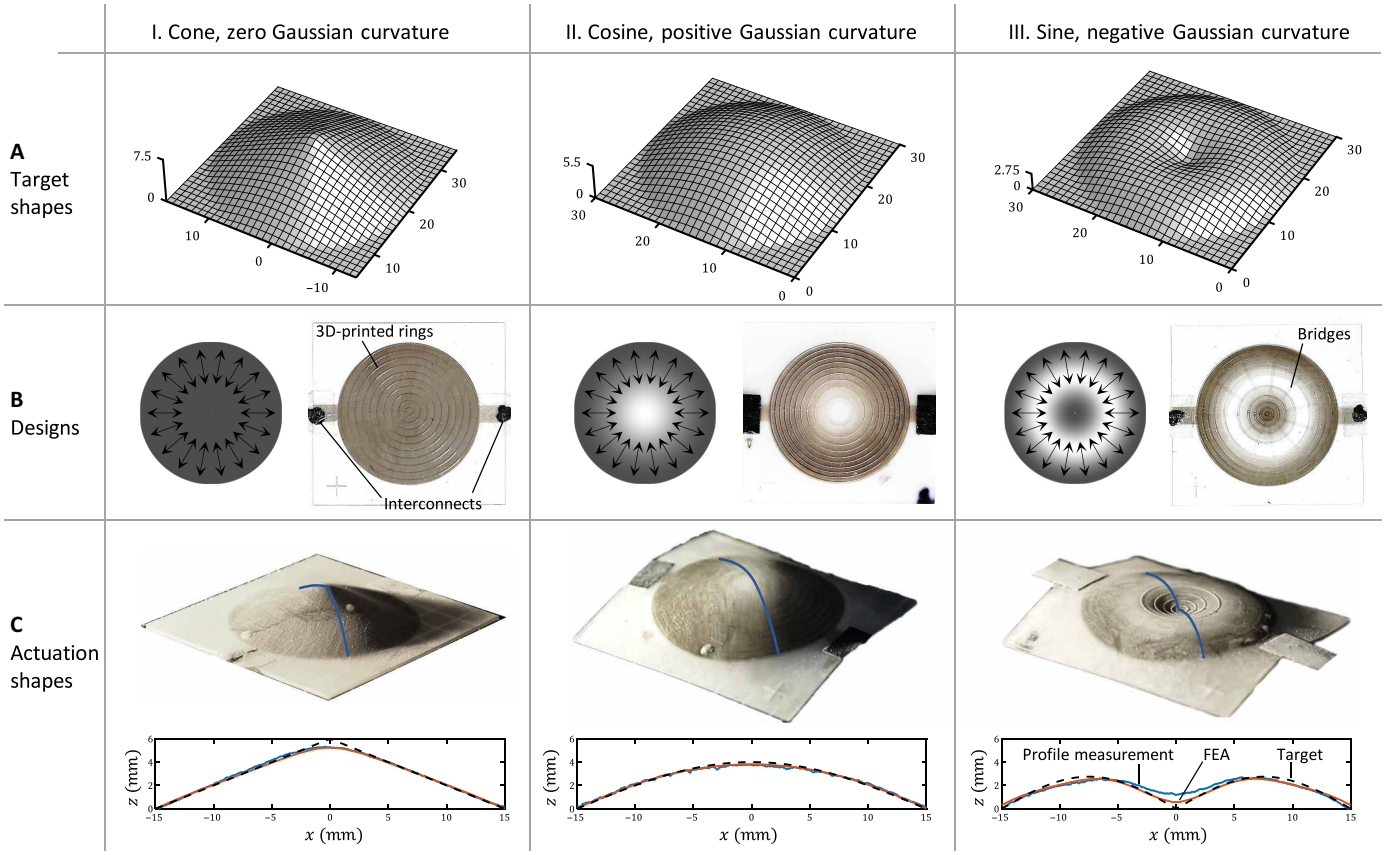

Fig. 2. Morphing into well-defined target shapes with zero, positive, and negative Gaussian curvatures, shown in columns I, II, and III, respectively. (**A**) The cone, cosine, and sinusoidal target shapes with zero, positive, and negative Gaussian curvatures, respectively. (**B**) The actuator designs for the three target shapes. The schematics on the left-hand side show the needed continuous actuation field to generate the target shape exactly, in which the arrows and color intensity represent the direction of the locally uniaxial actuation and the continuous number of active layers ($N \to \infty$), respectively. The images on the right-hand side show the fabricated DEAs approximating these deformation fields using 10 concentric stiff rings and 11 designed electrodes (12 total layers including two protective outer layers), in which the shade of gray represents the number of overlapping CNT electrodes, and the actuation direction is locally normal to the rings. (**C**) The actuation shapes for the three actuators. The images on the top are photographs of the actuated DEA and the graphs on the bottom compare the cross section of the actuation profiles (blue solid lines) to the target shapes (black dashed lines) and FEA (orange solid lines).

overlap with adjacent electrodes.) Furthermore, the rings near the center are 3D-printed onto the flipped side of the DEA film, since the displacement field at the center is reversed (z increases with radius) compared to the displacement field at the edge (z decreases with radius). Figure S5 shows that the actuation around the center would have been mirrored if the rings were printed on the same side everywhere. Defining the direction of the out-of-plane deformations by printing the rings onto one side or the other is only a secondary function of the rings, their main function being to define the in-plane direction of the actuations. Movie S2 shows reversible morphing into the sine shape at 1 to 2 Hz.

Complex target shapes: Morphing into a face

To illustrate that the shape-morphing DEAs can actuate into much more complex target shapes than the axisymmetric ones studied in the previous sections, it is demonstrated in this section that a flat sheet can be morphed into the shape of a face. The target shape, defined by the x, y, and z coordinates of 200 × 200 surface points, is shown in Fig. 3A. The pattern of the stiff, narrow strips was defined by the contour lines of the target shape, shown with black lines in Fig. 3B. Using Eq. (1, the local number of active layers was determined from the local magnitude of the gradient vector, shown using a color map in Fig. 3B. Fifteen strips were used to reproduce the local actuation directions. Twelve layers were used to reproduce the local actuation magnitudes. The design of each electrode is shown in fig. S6. Using this design, a DEA was fabricated (Fig. 3C), following the procedure outlined in Materials and Methods. When the voltage was applied to the electrode interconnects, the initially flat sheet of elastomer morphed into a 3D face (Fig. 3D) that closely resembles the target shape, demonstrating the DEAs' capability for morphing into complex predefined target shapes. Surface profile measurements reveal how the initially flat sheet of elastomer morphs into the target shape as the voltage increases (Fig. 3E). The overall actuation surface profile at 2.5 kV (Fig. 3E, left) mimics the profile of the target shape (Fig. 3E, right); however, the details with sharp changes in height are not captured accurately due to the bending effects. A contour plot of the error for the out-of-plane displacement, $e_z = z_{\text{actuation}} - z_{\text{target}}$, normalized by the maximum height of the target

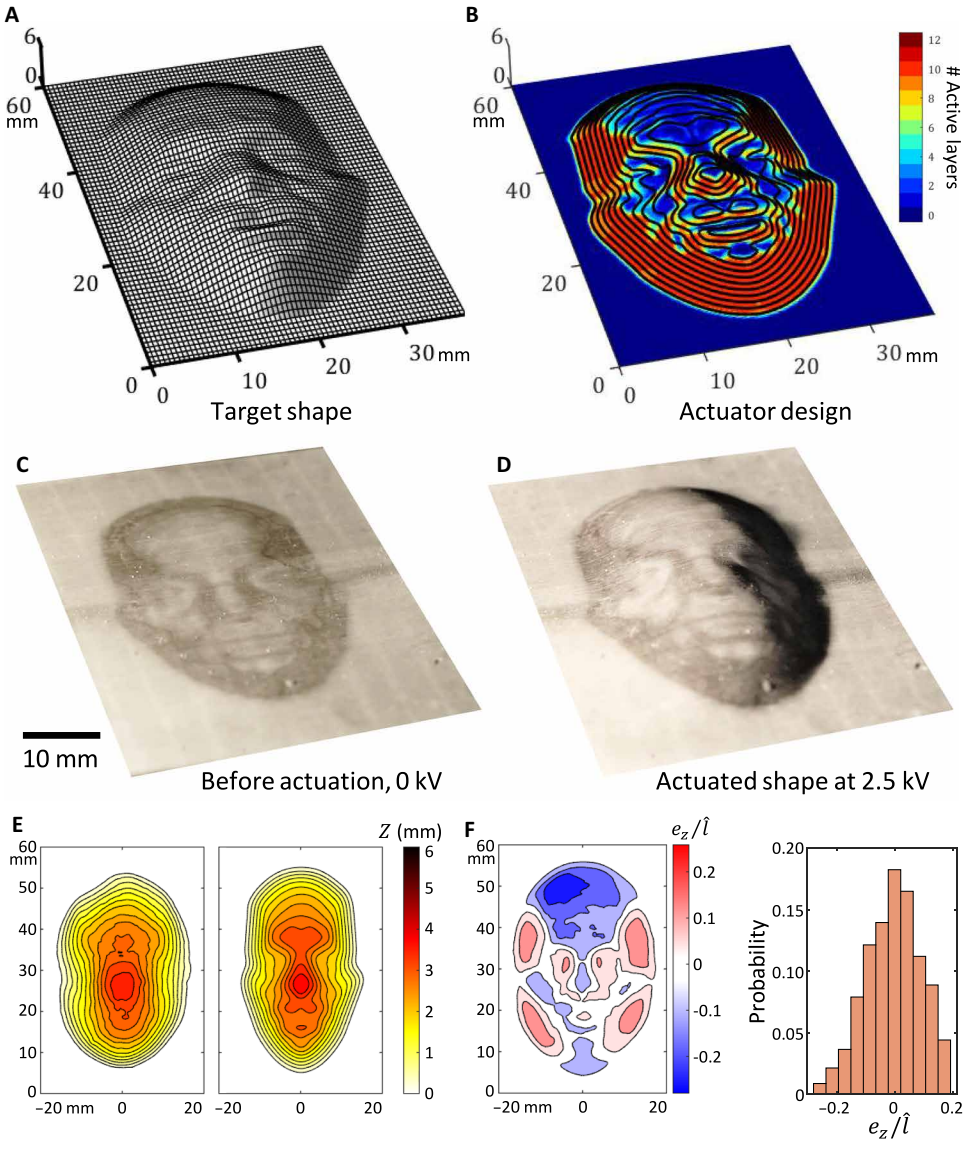

Fig. 3. Morphing into complex target shapes. (**A**) The target shape of a face is defined by 200 × 200 surface points. (**B**) The actuator design consists of 15 rings shown with black lines and 12 layers, for which the color map enumerates the local number of active layers. (**C**) Using this design, a shape-morphing DEA is fabricated. Before actuation, the DEA is flat, and the gray shadings are because of the local number of CNT electrodes. (**D**) When actuated by a voltage of 2.50 kV, the elastomer sheet morphs into a 3D face (right) that closely resembles the target shape. The light is shone from the left to use shadows for the visualization of the out-of-plane deformation of the actuation shape. (**E**) Height contour plots of the surface profile measurements of the initially flat DEA, actuated with applied voltages of 2.5 kV (left), compared to the target shape (right) shows their overall resemblance, but differences in details with sharper height changes. (**F**) Contour plots of the absolute error for the out-of-plane displacement, $e_z = z_{\text{actuation}} - z_{\text{target}}$, normalized by the maximum height of the target shape as the length scale $\hat{l}$ (left), and the probability distribution of the error (right), neglecting the zero displacement points ($z_{\text{target}} < 0.01$ mm).

shape as the length scale $\hat{l}$, is shown in Fig. 3F (left). The probability distribution of the normalized error is shown in Fig. 3F (right). While the errors are comparable to other programmed shape-morphing actuators, e.g., figure 5 in (*14*) showing a maximum error of ~8 mm when the maximum out-of-plane deformation is ~30 mm, the programmed shape-morphing DEAs described herein show fast and reversible response using applied voltages and are relatively insusceptible to their environmental conditions such as temperature. Movie S3 shows reversible morphing into the face shape at 0.5 to 1 Hz.

DISCUSSION

Implicitly, two limitations were imposed on the target shapes that DEAs can morph into: First, the target shapes must be defined by $(x, y, z(x, y))$; i.e., the shapes for which the out-of-plane height z is a function of the lateral positions x and y. A full sphere, for instance, cannot be defined in this manner. Second, the maximum gradient vector of the target shape is limited by the maximum actuation that the DEAs can produce before electrical breakdown. The DEA material used in this study shows a maximum uniaxial actuation of nearly 10% (fig. S2), which limits the steepness of the target shapes to

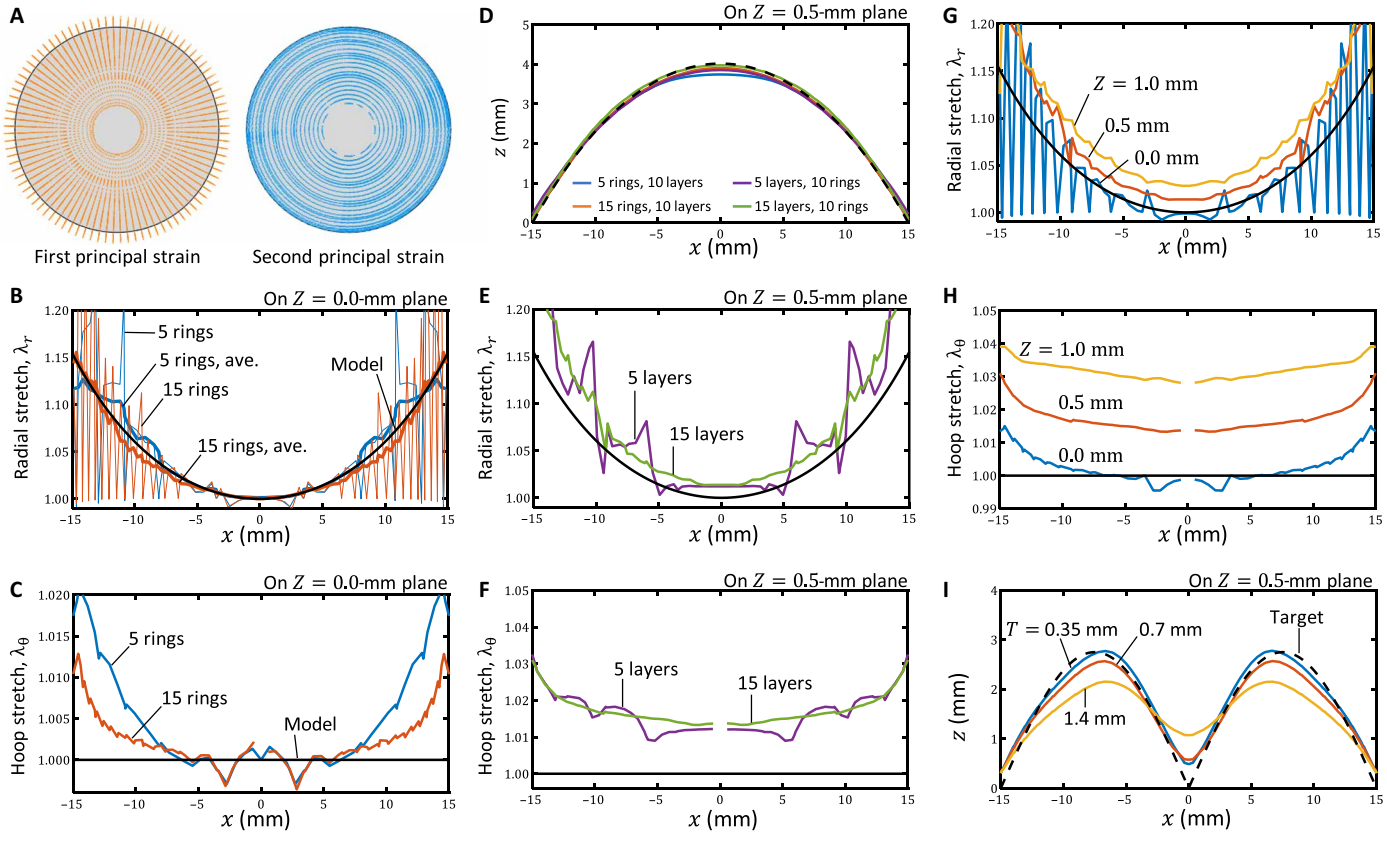

Fig. 4. Actuators with varying number of rings, layers, and thicknesses (FEA). (**A**) For a DEA with five rings and 10 layers, desgined to morph into the spherical cap of Fig. 1, the first and second principal strains are directed along the radial and hoop directions, respectively. (**B**) For two DEAs morphing into the spherical cap using 5 and 15 rings, both with 10 layers and a total thickness of 1 mm, the radial stretches are similar, better seen using the smoothed moving average curves, averaged over 10% of the diameter. (**C**) The required unity hoop stretch is better reproduced for the higher number of rings. (**D**) Actuation profiles for DEAs with 5 and 15 rings, both with 10 layers, and with 5 and 15 layers, both with 10 rings, compared to the target shape (black dashed lines). (**E**) Comparing the radial actuation of two DEAs with 5 and 15 layers, both with 10 rings, shows jumps in radial stretch for the DEA with 5 layers and smooth changes in radial stretch for the DEA with 15 layers. (**F**) The hoop stretch for the two DEAs with 5 and 15 layers has a similar offset from the model. (**G**) The radial actuation of a DEA with 15 layers, 10 rings, and a thickness of 1 mm, morphing into the spherical cap, shows the increase in radial stretch at the midplane, $z = 0.5$ mm, and top plane, $z = 1.0$ mm, of the elastomer sheet, compared to the bottom plane, $z = 0$, onto which the stiff rings are deposited. (**H**) Similar to the radial stretch, the hoop stretch shifts away from the model as z increases. (**I**) Actuation profile of three DEAs, one with the same thickness as the DEA in Fig. 2 (column III), one with twice the thickness, and one with half the thickness.

$|\vec{\nabla} z| = 0.46$, corresponding to a slope of 29°. Target shapes with greater steepness require DEA materials capable of larger actuations. For instance, for 60° slopes, an actuation strain of 100% would be required.

Three approximations were also made that can cause deviations of the actuation shapes from the target, two inherent to the shape-morphing method and one stemming from the simplifications used for the solution of the inverse problem. The shape-morphing method approximately reproduces the desired continuous spatial distribution of actuation magnitudes and directions using a few active and inactive layers and discrete stiff rings. The analytical solution of the inverse problem assumes that all the bending effects are negligible, including both the bending moments from the distribution of the active layers along the thickness and the bending stiffnesses. At the limit of infinite number of layers and rings, each infinitely thin, the continuous distributions of actuation magnitudes and directions can be exactly reproduced, and the bending terms will be zero. Therefore, the validity of the three approximations can be examined by increasing the number of layers and rings and changing the film thickness. This is done in the following using FEA that aids in visualizing not only the effect of number of layers, stiff rings, and thickness on the actuation profiles but also the internal stretch distributions. Examples of morphing into the spherical cap of Fig. 1 and sinusoidal shape of Fig. 2 (column III) will be demonstrated.

For the spherical cap of Fig. 1, the target actuation field as described by the analytical model is a continuous distribution of uniaxial actuation along the radius with zero hoop strain. Figure 4A visualizes the FEA results for the first and second principal strains on the midplane ($Z = 0.5$) of a DEA with five stiff rings and 10 layers designed to morph into the spherical cap of Fig. 1, showing that the first principal strain is everywhere directed along the radius, and the second principal strain, along the hoop direction, is much smaller than the radial stretch, although nonzero.

As the number of stiff rings increases, the continuously varying actuation direction is reproduced more accurately. For two DEAs that are designed to morph into the spherical cap using 5 and 15 stiff rings, both with 10 layers, Fig. 4 (B and C) shows the radial stretch, $\lambda_r = dx/dX$, and hoop stretch, $\lambda_\theta = x/X$, on the bottom plane of the elastomer ($Z = 0$) onto which the stiff rings are deposited. The

radial stretches under the infinitely thin, stiff rings approach unity, balanced by the stretches between the rings that are higher than the model. The analytical model assumes zero actuation strains in the hoop direction, which is better achieved with higher number of stiff rings (Fig. 4C). Although the stretch distributions for shape-morphing DEAs with 5 and 15 rings are different, both accurately morph into the target shape (Fig. 4D), at $\sqrt{(N-2)/N}\hat{\phi}_a = 0.78$, where $N = 10$ is the total number of layers and $\sqrt{(N-2)/N}$ accounts for the two inactive encapsulating layers. This shows that the actuation shape is not sensitive to the choice of the number of rings, provided that the rings are stiffer than the elastomer by three to four orders of magnitude. However, as shown in fig. S7, the actuation shape differs significantly from the target shape if both the stiffness of the rings and the number rings are small, e.g., if the rings are only 500 times stiffer than the elastomer and only five rings are used (fig. S7A).

As the number of layers increases, the continuously varying actuation magnitude is also reproduced more accurately. For two DEAs that are designed to morph into the spherical cap using 5 and 15 layers, both with 10 rings, Fig. 4 (E and F) shows the radial stretch and hoop stretch on the midplane of the elastomer ($Z = 0.5$ mm). When five layers are used, stepwise change in the radial stretch is observed, while the actuator with 15 layers shows smoother variation in the radial stretch. The hoop stretches have a similar offset from the model. Although the stretch distributions for the two DEAs are different, both accurately morph into the target shape (Fig. 4D) at $\sqrt{(N-2)/N}\hat{\phi}_a = 0.78$.

To examine the effects of bending, Fig. 4 (G and H) shows the radial and hoop stretches at the bottom plane ($Z = 0$), midplane ($Z = 0.5$ mm), and top plane ($Z = 1.0$ mm) of a DEA with 15 layers and 10 rings at $\sqrt{(N-2)/N}\hat{\phi}_a = 0.78$, designed to morph into the spherical cap. Because of the high stiffness of the rings, the neutral plane is located near the bottom plane of the elastomer ($Z = 0$), and both the hoop and radial stretches increase with Z due to the bending of the elastomer sheet.

As the elastomer thickness decreases, the bending terms become negligible, resulting in a better resolution of the target shape. This is clearly observed for target shapes having sudden changes in slope, for which the bending terms become significant, such as the singular point of the sinusoidal target shape of Fig. 2 (column III) at $X = Y = 0$. Figure 4H compares the actuation profiles when the thickness of the elastomer is twice and half of the elastomer sheet in Fig. 2 (column III). As expected, the DEA morphs into the target shape more accurately, when the thickness is decreased, making the bending terms less significant. Since there is a minimum to how thin each elastomer layer can be fabricated, reducing the total thickness of the actuator results in reducing the total number of layers. The optimum thickness of an actuator is, therefore, a compromise between the bending effects and the discretization quality of the continuously varying local actuations defined by the total number of layers.

In summary, morphing thin sheets of elastomer actuators into desired target shapes using an applied voltage has been realized by coupling inverse design with digital fabrication. We introduce a simple analytical solution to the inverse problem based on local control of uniaxial actuation directions and magnitudes within the internal architecture of the actuator. On the basis of these target designs, we then fabricated architected DEAs in which the number of active layers is locally programmed to control their actuation magnitude, while patterning stiff elements, such as rings or strips, using 3D printing is used to locally control their actuation directions. The versatility of this integrated strategy is demonstrated using actuators that transform from flat structures into shapes with zero, positive, and negative Gaussian curvatures as well as complex shapes, such as a human face. Compared to other shape-morphing materials reported in the literature, shape-morphing DEAs provide fast and reversible actuations that are impervious to their environment conditions, providing a unique solution for biomimicry of flying and swimming locomotion that require high–power density shape-morphing actuations. The limitations and approximations of the shape-morphing DEAs and the solution to the inverse problem were identified. For simple and smooth shapes, such as cosine and cosine cap, the error in out-of-plane actuations was negligible. While larger errors were measured for the more complicated shapes, such as a human face, these errors remain comparable to the other shape-morphing actuators previously reported in the literature. It is demonstrated that these limitations can be minimized by increasing the number of active layers and stiff elements while decreasing the elastomer thickness to minimize local bending. Together, these enabled the fabrication of architected elastomers that faithfully transformed into the desired target shape with excellent resolution of spatial features. Looking ahead, this will be instrumental for creating high-performance robots biomimicking the complex shape changes of swimming and flying locomotion, taking into account fluid-solid interactions.

MATERIALS AND METHODS

Architected DEA fabrication

Architected DEAs are fabricated by a layer-by-layer scheme. Each layer was fabricated by spin coating of a urethane acrylate–based precursor at 3000 rpm for 1 min, following a 15-s ramp-up at 200 rpm/s^2, leading to layer thicknesses of 60 μm. The precursor was made of 99.5% oligomer CN9028 (Sartomer Arkema Group) and 0.5% diphenyl(2,4,6-trimethylbenzoyl)phosphine oxide (Sigma-Aldrich) as the photoinitiator, mixed using a planetary centrifugal mixer (ARE-310, Thinky Mixer) at 2000 rpm for 20 min, followed by degassing using centrifugation at 8000 rpm for 20 min (Sorvall Primo Centrifuge, Thermo Fisher Scientific). The spin-coated layers were cured for 100 s under an array of six UV lamps with a peak intensity of 366 nm (Hitachi, F8T5-BL) inside a nitrogen chamber to prevent oxygen inhibition.

Following the procedure described in the appendix in (*3*), CNT electrodes are formed by vacuum filtration of 2 ml of a suspension of functionalized single-walled CNTs, 1 ± 0.5 μm long, in deionized water, with a concentration of 15 μg/ml, through polytetrafluoroethylene filter membranes with a 0.2-μm pore size (T020A090C, Advantec MFS Inc.) and a filtration area of 38.5 cm^2. This produces mechanically compliant CNT electrodes with a sheet resistance of 7 kilohms/□. The CNT electrodes were transferred onto the CN9028 elastomer layers using stamps that define the geometry of the electrodes. The stamps were made of Sylgard 184, at their stoichiometry ratio of 10A:1B, and the electrode geometries were cut out using a laser cutter (Universal Laser Cutter VLS 6.60). The sheet resistance of the CNT electrode was 10 kilohms/□ on the stamp, and 17 kilohms/□ after transferring onto the CN9028 elastomer surface. The sheet resistances were measured by the four-point probe method (*25*) using a Keithley 6221 current source and a Keithley 2182A Nanovoltmeter.

The stiff rings were made from a UV-curable acrylate-based viscoelastic ink. The ink was prepared by combining 9.5 g of E-Shell 300 Clear (EnvisionTEC) and 0.665 g of fumed silica (CAB-O-SIL M5,

Cabot Corporation). The components were mixed at 1800 rpm for 18 min (with 2 min breaks between every 2 min of mixing) in a SpeedMixer (FlackTek Inc.). After preparation, the ink was loaded into 10-cm^3 UV/light block amber syringes (Nordson EFD) and centrifuged. The ink was deposited onto the DEA surface via direct ink writing using a 100-μm nozzle (Nordson EFD) and a print speed of 1.5 mm/s. The motion of the printhead (ink and nozzle) was controlled by a 3D motion control system (Aerotech). The pressure applied to extrude the ink was controlled by an Ultimus V high-precision dispenser (Nordson EFD). Immediately following deposition along the prescribed print path, the printed features were UV-cured under flowing argon for 1 min using an OmniCure S2000 with a 320- to 500-nm filter option at a power level of 100.

Actuation and characterization of shape-morphing DEAs

Uniaxial tension tests in fig. S1A were performed on dog bone–shaped specimens with the geometrical parameters suggested by ASTM D412-16 (die C scaled by half). The specimens are stretched at a constant rate of 0.1 mm/s until rupture, and the tensile force was measured using a load cell (FUTEK LSB200, 2 lb, Jr. S-Beam Load Cell). To measure the stretch, the distance between two marks, drawn on the narrow part of the dog bone samples, 10 mm apart, was measured as the specimen was stretched. The distance between these marks was measured from images recorded using a camera placed 30 cm above the sample. The measured distance over the initial distance gives the stretch. By fitting the Gent model to the uniaxial stress-stretch curve, the shear modulus was determined to be 327 kPa. For the numerical analysis, however, the neo-Hookean model with a shear modulus of 327 kPa was used instead of the Gent model. The two models agree well for the relatively small strains for which the strain hardening effect is negligible, i.e., for the strains far from the rupture. Since the actuation strains in the dielectric elastomers studied here are only a fraction of the ultimate strain, the neo-Hookean model accurately describes the actuation of the dielectric elastomer sheets with less computational cost than the Gent model.

The dielectric constant of the elastomer was determined to be 8.0, characterized by fitting the equi-biaxial actuation equation (*3*) to the measurements in fig. S2A. Figure S2A shows the in-plane actuation of a multilayer DEA with 10 active layers and 2 inactive protective layers on both sides, as a function of the applied voltage. The thickness of each layer is 60 μm, measured using a confocal microscope. The equi-actuations were measured from images recorded using a camera placed 30 cm above the sample. The sample was held between two acrylic plates, 1 mm apart, to ensure that the actuations remain in-plane. Soft electrical breakdowns were observed as spikes in fig. S2A, resulting in self-clearing and formation of blisters that decreases the capacitance, shown in fig. S2B. The capacitance was measured using an LCR meter (Agilent E4980A) at 20 Hz in parallel circuit mode.

The tensile mechanical properties of the cured acrylate-based material used in the stiff rings were measured using an Instron 5969 Universal Testing Machine with a 500-N load cell. Printed filaments were tested under tension at a rate of 50 mm/min with an initial gage length of 30 mm. Cross-sectional areas of representative filaments were measured from untested sections of the filaments imaged with a Zeiss Discovery V20 microscope. Figure S1B shows the stress-stretch measurement for the stiff rings. Fitting a neo-Hookean model to the measurement data gives a shear modulus of 1.17 GPa, which is more than three orders of magnitude larger than that of the elastomer.

The DEAs were actuated using a high-voltage power supply (Trek 610E, Trek Inc.), and the actuation profiles were measured using a laser line scanner (MTI ProTrak, PT-G 60-40-58) and a precision linear stage (GHC SLP35, GMC Hillstone Co. and MicroFlex e100 servo drive), synchronized, and automated using a LabVIEW virtual instrument. The line scanner was mounted to the table, shape-morphing DEAs were placed onto the linear stage, and the voltage was ramped up in steps of 50 V. In each step, the surface of the elastomer was scanned by moving the linear stage at 5 $mm{\cdot}s^{-1}$ rate, while the voltage was constant, resulting in $>10^4$ points per cm^2 in 5 to 15 s. The lateral, x, and height, z, resolutions of the laser line scanner are <50 and <10 μm, respectively, and the longitudinal y resolution of the linear stage is 1 μm.

FEA of shape-morphing DEAs

Actuation of DEAs is a nonlinear, coupled multiphysics problem, mathematically described by the balance of forces and the Gauss's flux theorem, together with a proper set of boundary conditions and constitutive equations for the material models. Following the standard finite element formulation procedure (*3*), the governing partial differential equations are converted into a system of nonlinear algebraic equations. This system of nonlinear equations was then solved in Abaqus using Newton-Raphson's iterative method. An Abaqus user element (UEL) was developed to incorporate the coupling terms into the residual vector and stiffness matrix. Details of the finite element formulation and the UEL code are provided as the supplementary materials of (*3*).

SUPPLEMENTARY MATERIALS

Supplementary material for this article is available at https://science.org/doi/10.1126/sciadv.abn9198

REFERENCES AND NOTES

1. A. Hedenström, L. C. Johansson, Bat flight: Aerodynamics, kinematics and flight morphology. *J. Exp. Biol.* **218**, 653–663 (2015).
2. G. V. Lauder, E. J. Anderson, J. Tangorra, P. G. Madden, Fish biorobotics: Kinematics and hydrodynamics of self-propulsion. *J. Exp. Biol.* **210**, 2767–2780 (2007).
3. E. Hajiesmaili, D. R. Clarke, Dielectric elastomer actuators. *J. Appl. Phys.* **129**, 151102 (2021).
4. M. Duduta, E. Hajiesmaili, H. Zhao, R. J. Wood, D. R. Clarke, Realizing the potential of dielectric elastomer artificial muscles. *Proc. Natl. Acad. Sci. U.S.A.* **116**, 2476–2481 (2019).
5. Y. Chen, H. Zhao, J. Mao, P. Chirarattananon, E. F. Helbling, N. S. P. Hyun, D. R. Clarke, R. J. Wood, Controlled flight of a microrobot powered by soft artificial muscles. *Nature* **575**, 324–329 (2019).
6. G. Li, X. Chen, F. Zhou, Y. Liang, Y. Xiao, X. Cao, Z. Zhang, M. Zhang, B. Wu, S. Yin, Y. Xu, H. Fan, Z. Chen, W. Song, W. Yang, B. Pan, J. Hou, W. Zou, S. He, X. Yang, G. Mao, Z. Jia, H. Zhou, T. Li, S. Qu, Z. Xu, Z. Huang, Y. Luo, T. Xie, J. Gu, S. Zhu, W. Yang, Self-powered soft robot in the Mariana Trench. *Nature* **591**, 66–71 (2021).
7. M. Duduta, D. R. Clarke, R. J. Wood, A high speed soft robot based on dielectric elastomer actuators, in *Proceedings of the 2017 IEEE International Conference on Robotics and Automation (ICRA)* (IEEE, 2017), pp. 4346–4351.
8. G. Gu, J. Zou, R. Zhao, X. Zhao, X. Zhu, Soft wall-climbing robots. *Sci. Robot.* **3**, eaat2874 (2018).
9. S. Shian, R. M. Diebold, D. R. Clarke, Tunable lenses using transparent dielectric elastomer actuators. *Opt. Express* **21**, 8669–8676 (2013).
10. Y. Klein, E. Efrati, E. Sharon, Shaping of elastic sheets by prescription of non-Euclidean metrics. *Science* **315**, 1116–1120 (2007).
11. A. S. Gladman, E. A. Matsumoto, R. G. Nuzzo, L. Mahadevan, J. A. Lewis, Biomimetic 4D printing. *Nat. Mater.* **15**, 413–418 (2016).
12. J. Kim, J. A. Hanna, M. Byun, C. D. Santangelo, R. C. Hayward, Designing responsive buckled surfaces by halftone gel lithography. *Science* **335**, 1201–1205 (2012).
13. E. Siéfert, E. Reyssat, J. Bico, B. Roman, Bio-inspired pneumatic shape-morphing elastomers. *Nat. Mater.* **18**, 24–28 (2019).
14. J. W. Boley, W. M. van Rees, C. Lissandrello, M. N. Horenstein, R. L. Truby, A. Kotikian, J. A. Lewis, L. Mahadevan, Shape-shifting structured lattices via multimaterial 4D printing. *Proc. Natl. Acad. Sci. U.S.A.* **116**, 20856–20862 (2019).

15. X. Ji, X. Liu, V. Cacucciolo, M. Imboden, Y. Civet, A. E. Haitami, S. Cantin, Y. Perriard, H. Shea, An autonomous untethered fast soft robotic insect driven by low-voltage dielectric elastomer actuators. *Science Robotics* **4**, eaaz6451 (2019).
16. E. Hajiesmaili, D. R. Clarke, Reconfigurable shape-morphing dielectric elastomers using spatially varying electric fields. *Nat. Commun.* **10**, 183 (2019).
17. E. Hajiesmaili, E. Khare, A. Chortos, J. Lewis, D. R. Clarke, Voltage-controlled morphing of dielectric elastomer circular sheets into conical surfaces. *Extreme Mech. Lett.* **30**, 100504 (2019).
18. D. L. Henann, S. A. Chester, K. Bertoldi, Modeling of dielectric elastomers: Design of actuators and energy harvesting devices. *J. Mech. Phys. Solids* **61**, 2047–2066 (2013).
19. H. A. Eschenauer, N. Olhoff, Topology optimization of continuum structures: A review. *Appl. Mech. Rev.* **54**, 331–390 (2001).
20. F. Chen, K. Liu, Y. Wang, J. Zou, G. Gu, X. Zhu, Automatic design of soft dielectric elastomer actuators with optimal spatial electric fields. *IEEE Trans. Robot.* **35**, 1150–1165 (2019).
21. J. Martínez-Frutos, R. Ortigosa, A. Gil, In-silico design of electrode meso-architecture for shape morphing dielectric elastomers. *J. Mech. Phys. Solids* **157**, 104594 (2021).
22. R. Ortigosa, J. Martínez-Frutos, Topology optimisation of stiffeners layout for shape-morphing of dielectric elastomers. *Struct. Multidiscipl. Optim.* **64**, 3681–3703 (2021).
23. W. M. van Rees, E. Vouga, L. Mahadevan, Growth patterns for shape-shifting elastic bilayers. *Proc. Natl. Acad. Sci. U.S.A.* **114**, 11597–11602 (2017).
24. D. J. Struik, *Lectures on Classical Differential Geometry* (Courier Corporation, 1961).
25. L. B. Valdes, Resistivity measurements on germanium for transistors. *Proc. IRE* **42**, 420–427 (1954).

Acknowledgments

Funding: This work was supported by the National Science Foundation through the Harvard University Materials Research Science and Engineering Center DMR-2011754. We also thank ARO MURI (W911NF-17-1-03; N.L. and J.L.) for the partial support of this work. **Author contributions:** E.H. designed the research. E.H. and N.M.L. performed the research. E.H., N.M.L., J.A.L., and D.R.C. wrote the paper. **Competing interests:** D.R.C. and E.H. are inventors on a pending patent related to this work filed by Harvard University (no. US20210057632A1, filed 12 January 2018). The authors declare that they have no other competing interests. **Data and materials availability:** All data needed to evaluate the conclusions in the paper are present in the paper and/or the Supplementary Materials.

Submitted 30 December 2021
Accepted 2 June 2022
Published 15 July 2022
10.1126/sciadv.abn9198